Specific features of a stopped pipe blown by a turbulent jet: Aeroacoustics of the panpipes

Roman Auvray and Benoît Fabre
Lutheries-Acoustique-Musique–D'Alembert, Université Pierre et Marie Curie, Université Paris 06, Unité Mixte de Recherche, Centre National de la Recherche Scientifique 7190, Paris, France

Felipe Meneses and Patricio de la Cuadra[a)]
Centro de Investigación en Tecnologías de Audio, Pontificia Universidad Católica de Chile, Santiago, Chile

Pierre-Yves Lagrée
Institut Jean Le Rond d'Alembert, Université Pierre et Marie Curie, Université Paris 06, Unité Mixte de Recherche, Centre National de la Recherche Scientifique 7190, Paris, France

(Received 15 February 2016; revised 18 May 2016; accepted 18 May 2016; published online 28 June 2016)

Flute-like instruments with a stopped pipe were widely used in ancient cultures and continue to be used in many musical expressions throughout the globe. They offer great flexibility in the input control parameters, allowing for large excursions in the flux and in the geometrical configuration for the lips of the instrumentalist. For instance, the transverse offset of the jet axis relative to the labium can be shifted beyond the operational limits found in open-open pipes, and the total jet flux can be increased up to values that produce highly turbulent jets while remaining on the first oscillating regime. Some of the fundamental aspects of the acoustics and hydrodynamics of this kind of instrument are studied, like the instability of the jet wave and the static aerodynamic balance in the resonator. A replica of an Andean siku has been created to observe, through the Schlieren flow visualization, the behavior of both excitation and resonator of the instrument.
 [http://dx.doi.org/10.1121/1.4953066]

[AH] Pages: 3214–3225

I. INTRODUCTION

Many flute-like instruments form pre-Hispanic Latin America, especially those form the Andes region, share one common attribute: a resonator with a closed end. The most widespread species is the siku (also called zampoña, a name introduced by the Spaniards), and consists of several cylindrical stopped pipes attached together (Fig. 1). Its operation is similar in principle to that of stopped tubes in organ pipes or to that of Western panpipes. While the aesthetic emphasis in Western music is placed mainly on the organization of pitches, Andean musical excellence relies on the construction of a specific collective timbral texture which varies depending on the specific local culture and the particular type of festivity.[1] One key factor in the determination of this texture is the ceremonial character of the music; performances take place in open spaces, which requires loud sounds. Accordingly, pipes are blown with an extremely high jet flux. This results in the development of turbulence, associated with a strong wideband noise, both of which determine to a large extent the sound character of these instruments.

Most flute-like instruments whose sound production mechanisms have been well studied have open-open resonators and are commonly blown with laminar jets;[3] such is the case of the transverse flute, the recorder, and some registers of the organ pipe. Acoustics and fluid dynamics in stopped pipes have received comparatively little attention. In open-open pipes, the jet oscillates around the labium while the mean part of the entering jet (averaged over one period) induces a static flow through the pipe. Conversely, mass conservation in a stopped tube requires that the mean part of the jet flowing into the pipe must exit via the same place it entered: the blowing end. This results in a static component of the pressure gradient along the pipe and a subsequent steady component of the flow directed cross-stream to the jet. The jet flowing towards the labium crosses this area where it is deflected by the interaction with the crossflow (Fig. 2).

In contrast to the laminar case, turbulence induces a rapid spreading and slowing of the jet, which affects the velocity of convection of the acoustic perturbations; more specifically, it may affect the delay of convection of the perturbations from the flue exit to the labium, an important parameter for the auto-oscillation process.

FIG. 1. (Color online) Traditional cane siku composed of two rows of stopped pipes of different lengths and diameters.

[a)]Electronic mail: pcuadra@uc.cl

 0001-4966/2016/139(6)/3214/12/$30.00

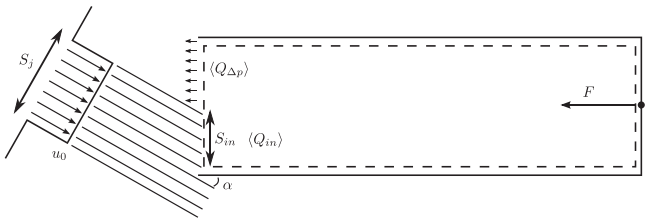

FIG. 2. Idealized scheme of a stopped pipe. Part of the flow goes into the resonator building up the pressure inside and creating a cross-stream that comes out from the tube and interacts with the jet.

This paper is structured as follows. Section II presents acoustic models in stopped pipes, including implications of turbulent jets and jets in crossflow. Fluid dynamic and acoustic models are developed for the purpose of interpreting data gathered from experiments on a laboratory replica of a siku. Possible modifications of the traditional flute model are also explored. Section III presents the experimental setup that makes it possible to obtain flow visualizations and pressure traces. Experiments are designed to test whether these types of instruments allow a wider range of control parameters (jet velocity, jet axis direction, and jet-labium offset) in order to produce stable oscillations. The results of these experiments are discussed in Sec. IV.

II. MODELING STOPPED PIPES EXCITED BY TURBULENT JETS

While turbulent jets and some aspects of stopped pipes have been studied independently, there is no evidence as to how their combination would modify the behavior in real instruments. Stopped-pipe instruments seem to tolerate a wider range of jet velocities while remaining in the first oscillating mode. Furthermore, it has been observed that the joint effect of turbulence and the steady crossflow may alter oscillations in the jet[4,5] and its velocity profile.

Figure 3 shows a scheme of the instrument with the variables describing its operation. The pressure difference between the mouth of the flautist and the channel exit leads

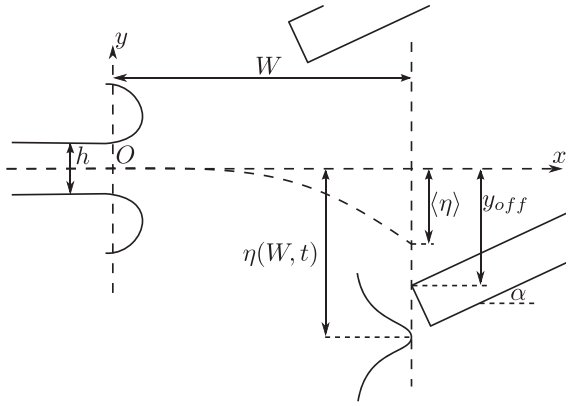

FIG. 3. Schematic view of the excitation part of a siku. The jet emerges from the "lips" at O, crosses the window of width W while being bent along the jet centerline $\langle\eta\rangle$ by flow recirculation. The x-direction is defined as the distance from the lip opening along the axis of the flue channel. The geometrical blowing conditions are characterized by the offset y_{off} between the jet axis and the labium, and the angle α between the jet axis and the pipe axis. During the auto-oscillation, the jet centerline $\eta(x,t)$ oscillates around its mean deviation $\langle\eta\rangle(x)$.

to the formation of a jet. The air flows through the short flue channel formed between the lips of the player and crosses a window of length W before reaching the labium. In resonant operation, this jet is perturbed by a transversal acoustic flow, mostly at its flow separation points at the flue exit.[3] Due to the intrinsic instability of the jet, this perturbation is amplified as it travels downstream. This results in the sinuous motion of the jet wave being phase-locked to the acoustic oscillations. When the wavy perturbation reaches the labium, the separation of the jet into two flows with complementary phases is usually described as an acoustic pressure source—a driving force for the oscillation of the column of air inside the resonator. The resonator amplifies the source near its resonant frequencies, creating the acoustic field, which closes the feedback loop.

Sound production in flute-like instruments is commonly modeled using lumped elements, where the interaction between successive elements in the loop is assumed to be local. This approach has been discussed in several papers and has been verified by numerous experimental studies.[6–10] Accordingly, our analysis is separated in two: the resonator and the excitation. Finally, the implications of the interaction of the two lumped elements in the real instrument are presented.

A. The resonator

1. Static pressure inside the pipe

A model for the static pressure build up in the pipe Δp is developed based on mass and momentum continuity along the pipe axis. For the analysis, a non-oscillating and inviscid—i.e., non-spreading—jet is assumed; the velocity profile is considered to have a top-hat shape. A smoother velocity profile would not fundamentally affect the following description, but it would result in a more complex set of equations. Oscillations are removed by averaging out all quantities over one period.

The flow entering the pipe over one period $\langle Q_{in}\rangle$ depends on the total flow coming from the flue $Q_0 = u_0 S_j$, the section $S_{in} = \sigma S_j/\cos\alpha$ of the fraction σ of the jet volume flux that enters the pipe, and the angle of the jet α:

$$\langle Q_{in}\rangle = \iint_{S_{in}} \mathbf{u}\cdot\mathbf{ds} = \sigma u_0 S_j, \tag{1}$$

with S_j the section of the jet as sketched in Fig. 2.

The flux leaving the pipe due to recirculation is

$$\langle Q_{\Delta p}\rangle = S_{\Delta p} u_{\Delta p}, \tag{2}$$

where the velocity of the outgoing flux $u_{\Delta p}$ is assumed to be uniform across the pipe cross section S_{pipe}, passing through the jet. Considering the mass continuity equation $\langle Q_{in}\rangle = -\langle Q_{\Delta p}\rangle$ yields

$$u_{\Delta p} = -\frac{\sigma S_j u_0}{S_{pipe}}. \tag{3}$$

The momentum continuity equation along the pipe axis for an incompressible flow is

$$-\rho_0\langle Q_{in}\rangle u_0\cos\alpha-\rho_0\langle Q_{\Delta p}\rangle u_{\Delta p}=F, \tag{4}$$

where F is the force exerted by the bottom of the pipe on the fluid. Using Eqs. (1) and (3) and expressing the force as a difference in pressure, relative to the surrounding pressure, $\Delta p=-F/S_{pipe}$ yields

$$\frac{\Delta p}{\rho_0 u_0^2}=\sigma\left(\frac{S_j}{S_{pipe}}\right)^2\left(\cos\alpha-\sigma\frac{S_j}{S_{pipe}}\right). \tag{5}$$

This rough estimation of the pressure build up at the closed end will be compared to measurements introduced in Sec. IV.

B. The excitation

It has been suggested[2] on theoretical grounds that the fluid dynamic balance in stopped pipes produces an auto-direction effect of the jet towards the labium. In other words, there is no need to aim the jet sharply at the labium; this makes it easier to produce a sound.

Just as in open-open tubes, the flow going into a stopped pipe Q_{in} can be decomposed into its mean $\langle Q_{in}\rangle$ and oscillatory Q'_{in} components. However, in this case the mean flow $\langle Q_{in}\rangle$ should exit through the same place it entered: the blowing end. This results in a crossflow with a static component that interacts with the jet, and a static pressure build up Δp at the closed end. Both aspects are analyzed in the following.

1. Jets in crossflow

Jets in crossflow have been studied by a number of authors[11–16] in the context of their work on industrial applications. In the case of the siku, the crossflow is generated by the jet itself and corresponds to the recirculation of the injected mean flow $\langle Q_{in}\rangle$. The ratio r, defined as the jet central velocity over the crossflow velocity, is greater than 1 for the sikus, since the jet cross section is smaller than or equal to the opening of the pipe.

For such a ratio, the flow might be slightly affected ($r\gg 1$) or strongly perturbed ($r\sim 1$). In the latter case, shear layers instabilities increase from the flow junction area (near the nozzle exit) to an extremely unsteady flow area.[14] The development of the shear layer instabilities makes the momentum of the jet and the crossflow—initially different—to mix while traveling downstream. The shape of the flue exit is also a crucial parameter that affects the development of the shear layer instabilities,[16] and thus the mean deflection.

In most configurations found in the literature, the crossflow is assumed to be fully developed in a semi-infinite space. Moreover, the literature is commonly interested in the interaction of the jet with the grazing flow involving a fully developed boundary layer. In the present case the boundary the Reynolds number of the crossflow $\mathrm{Re}_{crossflow}=\sigma\mathrm{Re}_{jet}$ therefore the crossflow is expected to be mostly turbulent. In the case of the siku, the geometry of the junction area is relatively intricate and varies from one musician to another. Moreover, the information usually studied, such as the modification of the jet velocity profile or the development of different kinds of vortices, is not necessary for the level of accuracy required by the present model. Hence, the effect of the crossflow is assumed to be described only by a mean deflection of the centerline $\langle\eta\rangle$ on top of which oscillations η' take place. Thus, the total displacement of the centerline as a function of the distance x from the lip opening is

$$\eta(x,t)=\eta'(x,t)+\langle\eta\rangle(x). \tag{6}$$

We propose to describe the jet deflection with the x dependence (inspired by research on round jets emerging from a plane wall[11]),

$$\frac{\langle\eta\rangle}{rh}\sim\left(\frac{x}{rh}\right)^{\delta}. \tag{7}$$

According to different configurations found in the literature, the order of magnitude of the amplification coefficient δ is greater than, but on the order of, 1.

2. Jet spreading and slowing

A jet emerges at $x=0$ with a velocity profile contingent on the history of the flow in the formation channel and on the shape of the flue exit. If the channel is short enough, the profile will assume a top-hat shape. The jet gradually smoothens due to the viscous entrainment of the surrounding fluid. At a distance l_e from the flue, the jet is considered to be fully developed and assumes a self-similar velocity profile. From there onwards, the self-similarity of the velocity profile yields

$$u(x,y)=u_{max}(x)f(y/b(x)), \tag{8}$$

where f is the self-similar profile and where the characteristic vertical distance b and the centerline velocity u_{max} are both functions of the distance x; they describe the spreading and the slowing of the jet, respectively.

In turbulent jets, both the spreading and slowing behave different from laminar jets.[17] affecting the velocity profile and the phase velocity of the perturbation c_p. Turbulent viscosity partially explains the fact that turbulent jets dissipate energy more rapidly than laminar jets.

In the case of fully developed turbulent free jets,[17] x-momentum conservation implies $bu_{max}^2=$ constant while due to the absence of other length scale $b/x=$ constant, so that $b\sim x$ and $u_{max}\sim b^{-1/2}\sim x^{-1/2}$. Based on the observations of several authors,[18] the centerline velocity is assumed to be constant prior to l_e. This leads to

$$u_{max}(x)=\begin{cases}u_0 & \text{if } x\le l_e\\ u_0\sqrt{\dfrac{l_e}{x}} & \text{if } x>l_e,\end{cases} \tag{9}$$

where u_0 is the centerline velocity of the initial velocity profile.

As the jet evolves in a crossflow it changes its velocity distribution due to momentum transfer, and its profile may

significantly differ from the self-similar shape. However, the crossflow is assumed to be relatively weak as compared to the jet ($r \gg 1$), so that the jet is well described by the self-similar assumption.

3. Jet instabilities

Work on the linear stability analysis of infinite parallel flows was initiated by Rayleigh. Despite the unrealistic assumptions of his analysis, it provides some insights into the instability mechanisms. Basically, a time harmonic excitation gives rise to two harmonic unstable modes, varicose and sinuous, defined by a symmetric and antisymmetric displacement of the two shear layers delimiting the planar jet.[19] In flute-like instruments the jet emerges cross-stream to the acoustic velocity field: the sinuous mode is dominant because of the strong antisymmetric excitation.

The relevant parameters provided by the stability analysis of parallel flows are the phase velocity c_p and the spatial growth rate α_i of the time-excited perturbation as functions of the Strouhal number and the self-similar velocity profile. The former determines the convection delay of the perturbation and thereby the oscillating frequency. The latter is directly related to the amplification of the oscillation and therefore to the triggering of nonlinear processes. For spreading jets, as the velocity profile evolves along the downstream direction, the two parameters c_p and α_i become functions of the downstream distance x too.[20] However, this level of accuracy exceeds the one in standard flute-like instrument modeling, where c_p and α_i are typically assumed constant, even with respect to the Strouhal number.

For laminar jets, experimental investigations validated the linear description of the perturbation, as a propagative transverse oscillation of the jet centerline,[21]

$$\eta'(x,t) = e^{\alpha_i x}\eta_0(t - x/c_p), \tag{10}$$

where the receptivity η_0 is a key parameter which reflects the modulation of the shear layers at the flow separation points of the jet due to the acoustic field. The receptivity is an empiric formulation that does not have a physical meaning: the jet centerline cannot be displaced at $x = 0$. The formula is valid only for a few characteristic distances h downstream, and shows reasonably good agreement with experimental data using

$$\frac{\eta_0}{h} = \frac{v_{ac}}{u_0}, \tag{11}$$

where v_{ac} is the harmonic transverse acoustic velocity at the flue exit. The parameters of convection velocity and amplification of the jet wave are defined as $c_p = \gamma u_0$ and $\alpha_i = \beta/h$, respectively, where $\gamma \sim 0.4$ and $\beta \sim 0.3$ in laminar jets.[22]

Studies on the instabilities of jets describe the transition from laminar to turbulent regime as triggered by the spatial amplification of spontaneous oscillations due to the instabilities in the shear layers.[17] In the case of synchronized oscillations, such as in edge-tone or flute configuration, turbulence may be triggered by the spatial growth of the perturbed jet. Indeed, when the amplitude of oscillation is large enough, nonlinear mechanisms are predominant. The vortices formed by the Rayleigh instability give rise to large scale structures in the turbulent flow.

Using particle image velocimetry on a turbulent jet in an edge-tone configuration, Lin and Rockwell[23] showed that large-scale patterns of vorticity are phase-locked with the measure of pressure on the tip of the edge. These large-scale patterns are of the same order as the hydrodynamical wavelength in a laminar case. Thus, the associated acoustic frequency is expected to be of the same order as the frequency in a laminar edge-tone. Lin and Rockwell also observed small-scale patterns of vorticity with no specific phase relation with the jet oscillation nor with the pressure measurement. These patterns of much smaller hydrodynamical length scale contribute to the production of broadband noise, a characteristic of turbulence: high frequency broadband noise with an absence of phase correlation with the large scale oscillation.

As for the modeling of the spreading and slowing of the jet, the contribution of the non-correlated vorticity patterns can be integrated into a simple model—similar to the laminar case—with an effective viscosity due to small-scale eddies interaction. Disregarding small fluctuations, the transverse displacement of the jet is assumed to be well approximated by Eq. (10) with values of the critical parameters η_0, c_p, and α_i, which may differ from those of the laminar case though they are expected to be of the same order of magnitude.[5]

Oscillation of turbulent jets forced by an acoustic transverse excitation have already been studied by Thwaites *et al.*,[18,24] and de la Cuadra *et al.*[5] They found that the phase velocity roughly behaves as $c_p \sim x^{-1/2}$ due to the decay of the centerline velocity as expected for a self-similar turbulent planar jet. Concerning the amplitude of oscillation, the initial part of the jet is well approximated by an exponential growth with a factor $\beta \sim 0.4$. Beyond a certain length, the amplitude of oscillation will exceed the half-width, and the growth of the perturbation will no longer be linear.[24]

4. Overblowing

The delay of the perturbation on the jet is critical in determining the oscillating frequency.[6] Sound production is optimal for a convection delay τ_c close to half the oscillating period T.[10,22] Since the perturbation travels at about γu_0, sound production is optimal for a Strouhal number $St_w = fW/u_0$ close to $\gamma/2$ (when $\tau_c = W/\gamma u_0$ equals $1/2f$).

Modifications on the total delay, caused by a slower convection of the perturbation in turbulent jets, also affect the overblowing mechanisms of the instrument. Oscillations are possible within a critical range around the optimal value. Values of the Strouhal critical range in experimental results from various authors are indexed in Table I. The lower limit of the Strouhal number corresponds to the critical value at which the system overblows, roughly close to a third of the optimal value. It should be noted that the mechanisms that trigger the regime change have not been fully understood, although some of them have been identified,[22] and that the evidence presented here is of an experimental nature.

TABLE I. Strouhal ranges that allow oscillation from different experimental results, on different types of flute.

	Lower limit	Optimal value	Upper limit
Verge *et al*. (Ref. 25)	0.07	0.17	0.25
Ségoufin *et al*. (Ref. 26)	0.07	—	0.25
de la Cuadra *et al*. (Ref. 27)	0.07	—	0.3
Auvray *et al*. (Ref. 22)	0.06	0.20	0.4

When the convection delay becomes too small because of an increase in the jet velocity, the Strouhal number decreases below its critical lower limit and the system changes its oscillating regime to match the next mode of the resonator. In other words, in an open-open pipe sounding in its first regime, an increase in the jet velocity beyond the critical value would result in an overblowing of the system on the second mode, thereby doubling the frequency. Thus, the balance of delays remains within the critical range, as does the Strouhal number.

It is well known that in stopped pipes the frequency ratio of the resonances are approximately in the ratio of the odd integers, with the result that, when the jet frequency is close to the first resonance, odd harmonics fall near resonances and become significantly stronger than the even harmonics. Moreover, overblowing a stopped pipe would produce a mode shift, jumping to a frequency close to three times that of the fundamental. One might expect the critical range to be extended due to the enlargement of this frequency interval.

The balance of delays may also be modified by one of the effects of the turbulence: the spreading of the jet is expected to modify the phase velocity of the perturbation,[20] and thereby the convection delay. The total delay should be integrated over the window distance W with the local phase velocity γu_0 where γ is a function of the downstream distance x. However, this description exceeds the accuracy of current models since the exact evolution of the jet velocity profile is required to compute the local phase velocity. A more general approach which still accounts for the slowing of turbulent jets and finds support in experimental observations[5,18] would be to consider an effective Strouhal number defined as

$$St^* = \int_0^W \frac{f\,dx}{u_{max}(x)} = \int_0^{l_e} \frac{f\,dx}{u_0} + \int_{l_e}^W \frac{f\,dx}{u_0\sqrt{x/l_e}} = \frac{f l_e}{3u_0}\left(2\left(\frac{W}{l_e}\right)^{3/2} + 1\right). \quad (12)$$

For fully turbulent free jet the origin of the self similar part may appear upstream from the flue exit. For this article St^* will be used as an indicator of the regime changeability.

III. EXPERIMENT

A laboratory replica of a siku was built with the modifications necessary to allow proper visualization and further analysis of images. The experiments seek to validate the parameters of the models proposed in Sec. II, including a detection of the jet centerline $\eta(x,t)$ for the analysis of the mean deflection $\langle\eta\rangle$ and the instability jet wave $\eta'(x,t)$, and the establishment length l_e. An acoustical analysis of the sounds obtained is also included.

A. Setup

The control parameters of the experiments are the jet-pipe angle α and the Reynolds number $\mathrm{Re} = u_0 h/\nu$, varied through the jet velocity u_0—for a flue of height h and a fluid of viscosity ν (for CO_2, $\nu = 8.1 \times 10^{-6}\mathrm{m}^2/\mathrm{s}$). Pure CO_2 was blown into the pipe for visualization purposes.

The replica is an aluminum tube with a square section: an inner cross-sectional area of $0.67\,\mathrm{cm}^2$ and an inner length $L_{pipe} = 9.76\,\mathrm{cm}$. These dimensions were chosen using the power law traditionally found in panpipes[2] (in centimeters): $D_{eq} = 0.35(L_{pipe})^{0.43}$, where D_{eq} is the diameter of a circumference of equivalent surface as the inner section of the pipe. The pipe is assumed to be uniformly filled with pure CO_2, providing a fundamental frequency in CO_2 of $f_0 = c_0/4L_{pipe} = 686\,\mathrm{Hz}$ with the speed of sound $c_0 = 268$ m/s. The stopped end is closed by a rubber cork with an Endevco dynamic pressure sensor model 8507C-2 mounted flush on it. In the region near the open end, two opposite walls were cut off and replaced with two larger pieces of transparent glass to make a visualization area (see Fig. 4).

The flue is made of a cylindrical brass tube of inner diameter 4.8 mm whose end has been flattened, cut and bent to resemble lips. The flue exit is 7 mm wide and $h = 0.7$ mm high, yielding a cross-section $S_{flue} \simeq 4.9\,\mathrm{mm}^2$. A 1 cm wide, 5 cm long, and 3 mm thick rubber piece was used to seal the gap between the flue and the edge of the pipe opposite the labium, an area that is normally filled by the jaw or lower lip of the instrumentalist.

The pipe and the nozzle are mounted on a system that allows for the variation of the flue-labium distance W, and the jet-pipe angle α. The radius W, chosen empirically to give optimal sound production, is set at 9.3 mm.

The pure CO_2 jet is regulated using a Brooks mass flow controller. Between the controller and the nozzle the flow passes through a settling chamber of volume $2.5 \times 10^{-3}\ \mathrm{m}^3$, where the velocity is taken to be zero and the pressure is measured using an Endevco dynamic pressure sensor model 8507C-2. The cavity is connected to the nozzle by a plastic tube of inner diameter $D = 6.2$ mm and length $L = 2.5$ m. This allows for a complete development and stabilization of the velocity profile in the tube; however, viscous losses are significant and cannot be disregarded. Consequently, a specific model is developed for the estimation of the velocity at the flue. The jet velocity is estimated by applying the law of

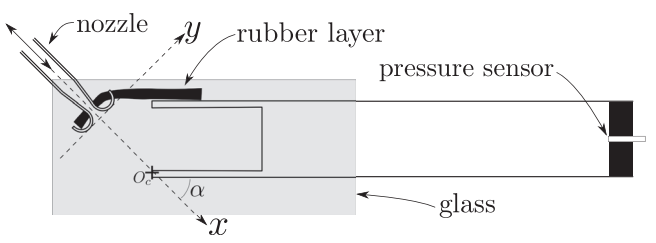

FIG. 4. Sketch of the experimental setup. The nozzle can rotate around the center O_c and can be translated along the x and y axes.

Blasius. For a turbulent flow in a cylindrical pipe of length L, the pressure drop P_{drop} between the cavity and a point just before the constriction of the nozzle is given by[28]

$$\frac{P_{drop}}{L} = \lambda \frac{\frac{1}{2}\rho_0 u^2}{D}, \tag{13}$$

where u is the centerline velocity just before the constriction of the nozzle, ρ_0 the density of the fluid (for CO_2, $\rho_0 = 1.8\,\mathrm{kg/m^3}$) and $\lambda = 0.316\mathrm{Re}_D^{-1/4}$ the friction coefficient, with the Reynolds number $\mathrm{Re}_D = uD/\nu$ and the viscosity ν. The jet centerline velocity at the nozzle u_0 can be estimated by applying mass conservation ($uD^2\pi/4 = S_{flue}u_0$) and energy conservation (Bernoulli) between the points just before and after the constriction.

In addition to the internal pressure measurements, a B&K 4938 microphone captures the radiated pressure at a point set 29 cm away from the labium (9 cm above the labium in the axial direction of the pipe, 19 cm in the direction perpendicular to the x-y plane, and 20 cm in the direction perpendicular to the pipe axis and parallel to the x-y plane).

Visualization is achieved by blowing CO_2 for all the experiments and using the Schlieren photography technique. Images are captured at 8 Hz with a shutter speed of 100 ns. Additionally, the camera provides an analog synchronizing signal independent of the pressure oscillation. A typical image of the experiment is shown in the Appendix. Since the pipe is saturated with CO_2, the mass gradient of the inner shear layer of the jet is less pronounced, causing a weaker contrast in the flow visualization.

B. Experiments

Each experiment covers the acquisition of 368 images ($\sim$ 46 s) under steady conditions of the control parameters α and $\mathrm{Re} = u_0 h/\nu$. A total of 20 measurements are performed, covering five jet angles (24°, 36°, 46°, 57°, and 69°) and four Reynolds numbers ($\sim$ 2400, 3000, 4300, and 5200) corresponding to four jet velocities ($\sim$ 28, 35, 50, and 60 m/s). In all cases the jet has a laminar and a turbulent region, with a transition around 3 mm downstream from the flue.

All concluding remarks in this investigation are retrieved from this set of 20 experiments. Nonetheless, in an attempt to determine whether the jet auto-directs towards the labium, as suggested by Fletcher,[2] three additional measurements were performed by shifting the offset $y_{off} \simeq 3$ mm, thus aiming the jet at the center of the bore. Using this configuration, three angles (24°, 36°, 46°) were tested with $\mathrm{Re} \simeq 4300$ (jet velocity of $\sim$ 50 m/s).

For an average range of $\mathrm{Re} \simeq 2400$ to 5200, the variation of other relevant quantities is as follows: fluctuating pressure at the closed end p', 143 to 159 dB; radiated pressure, 75 to 93 dB; pressure difference in the pipe Δp, 40 to 240 Pa; pressure in the upstream cavity p_{cavity}, 1000 to 4500 Pa; and mass flow controller output, 1.4×10^{-4} to 2.9×10^{-4} m^3/s.

C. The processing of images

The images present several challenges from the viewpoint of the analysis. For instance, one of the control parameters is the jet-pipe angle, which means that the geometrical configuration changes constantly. Thus, processing is needed in order to define a homogeneous window of observation, such as the one in Fig. 3. Furthermore, the video frame rate is low (8 Hz) and is not synchronized with the oscillation frequency of the jet ($\sim$690 Hz), so that no direct representation of motion can be deduced from the images. Finally, small vortex structures make the detection of the centerline difficult. A detailed explanation of the algorithmic procedure is presented in the Appendix.

The oscillating pressure at the closed end of the pipe p' is used as a reference for the harmonic motion of the jet. The signal is linked to the synchronizing signal of the camera. Each image is labeled with the acoustic phase position at the moment of the capture. The original size and orientation of the images is cropped and rotated using the nozzle structure as a reference in an image registration algorithm.[29] Then, as a way of reducing the effects of turbulence, smoothed images that average information from several phase-adjacent images are created. These are called "aggregated" to differentiate them from the original "single-shot" ones. Finally, a simulated period of oscillation is created by uniformly selecting 32 images in the range $[0 - 2\pi]$. This is done for both single-shot and aggregated images.

A modified version of the cross-correlation algorithm proposed by de la Cuadra[5] was used to detect the centerline $\eta(x,t)$. Aggregated images are used for this purpose because the turbulence makes it impossible to use single-shot ones. Fourier analysis of $\eta(x,t)$ is performed in order to obtain the mean deflection $\langle\eta\rangle$ of the jet, and the amplitude $|\eta'|$ and phase $\phi_{\eta'}$ of the jet wave. Curve fitting is then used to extract the mean deflection coefficient δ and the amplification factor of the jet wave α_i. The establishment length l_e is obtained by running the centerline detection algorithms on single-shot images, and measuring the point where the two turbulent shear layers collapse.

IV. RESULTS

A. The resonator

The pressure difference at the closed end of the tube Δp is compared to the model developed in Sec. III [see Eq. (5)]. Results are displayed in Fig. 5. The pressure difference slightly increases as the angle decreases (i.e., as the jet aligns itself with the pipe axis). The prediction of the model overestimates the pressure decay with the angle but provides the same order of magnitude and the same trend. However, the model does not predict a Reynolds number dependence, though it was experimentally observed. The adjustable parameter σ has been set to 0.6 to match experimental observation, making it possible to estimate the fraction of the jet which enters the pipe and therewith the ratio r of the jet velocity over the crossflow velocity [see Eq. (3)]: for all the experiments, r has been found to be on the order of 23 except for the three experiments where the offset $y_{off} \simeq 0.3$ mm, σ being set to 1.

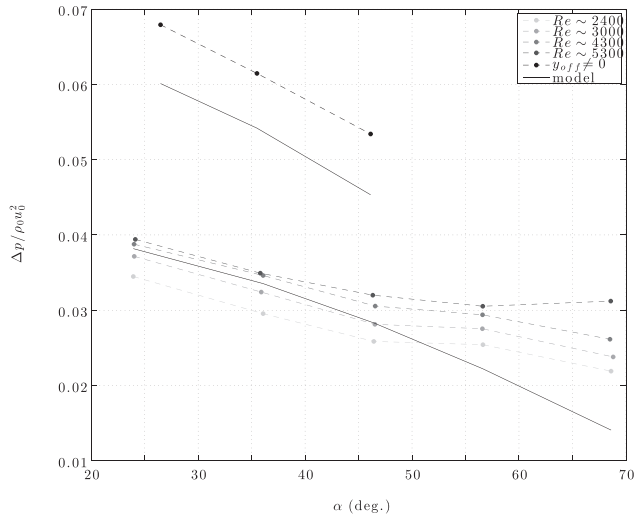

FIG. 5. Dimensionless pressure difference at the closed end $\Delta p/\rho_0 u_0^2$ versus angle of the jet α for different flow commands (solid line: model developed in Sec. II A 1; dashed line: experimental data). The parameter fraction of jet that enters the pipe σ is set to 0.55 for the case $y_{off}=0$ and 0.95 for the case $y_{off} \neq 0$.

B. The excitation

1. Jets in crossflow

The detection of the instantaneous deflection of the centerline $\eta(x,t)$ using aggregated images is shown in Fig. 6 (blue straight line). The mean deflection of the centerline $\langle\eta\rangle$ (red dotted line) is also shown and evidences the deviation from the x axis of the average oscillation. Results of $\langle\eta\rangle$ show the expected behavior for a jet in a crossflow given by Eq. (7), but only in the first half of the jet. In the second half, the shifting tendency seems to cease; the mean position of the centerline remains in the vicinity of the displacement achieved in the first half. The jet deflection has been fitted with the function $\langle\eta\rangle/rh = a(x/rh)^{\delta}$ on the first half of the window ($x \in [0, W/2]$). Figure 7 shows values of δ. Except for the very critical case $\alpha = 69°$ (with jet almost orthogonal to the pipe axis), all the δ values are close to 2. No specific trend for δ with the Reynolds number, nor with the angle α, has been found.

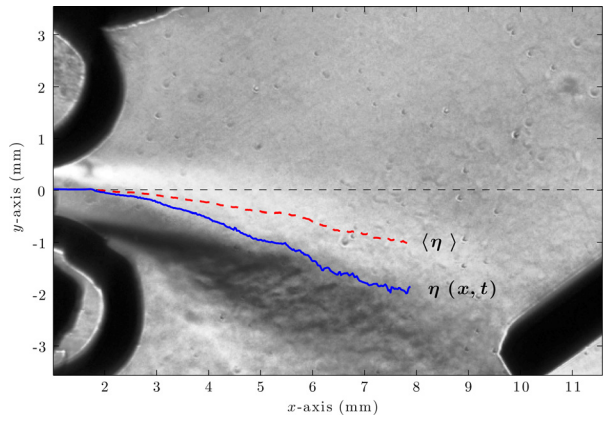

FIG. 6. (Color online) Detected instantaneous deflection $\eta(x,t)$ (straight line) and mean deflection $\langle\eta\rangle$ (segmented line) of the centerline of the jet in an aggregated image, for $\varphi = 146.25°$, $y_{off} \simeq 3$ mm, and (Re,α) = (4300,36°).

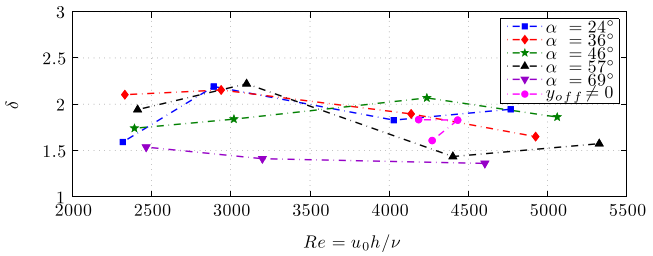

FIG. 7. (Color online) Coefficient δ of the steady deflection of the jet $\langle\eta\rangle/h = a(x/h)^{\delta}$ versus Reynolds number $\mathrm{Re} = u_0 h/\nu$ for all the blowing conditions. When not specified in the legend, the offset y_{off} is null.

The total jet displacement at the labium is small, $\langle\eta\rangle(W) \simeq 0.35$ mm. Nevertheless, for the three experiments where the offset is changed to $y_{off} \simeq 3$ mm, the tendency $\langle\eta\rangle \sim x^{\delta}$ is maintained throughout the entire jet length. Values of δ for this case are also displayed in Fig. 7. The total displacement is now $\langle\eta\rangle(W) \simeq 1$ mm, so that the jet does not oscillate around the labium but around a point two millimeter is above it.

The mean deflection of the jet centerline due to air recirculation within the pipe seems to act therefore only on the first half of the jet. When the jet is directed to the labium, the resulting deflection at the labium is small compared with the open-open pipe case. But when the jet is not directed at the labium but towards the center of the pipe inlet, the mean deflection makes the jet bend back toward the labium, providing a total deflection that is, on average, three times higher than that of the former case. The mean jet centerline position is almost entirely fixed by the aerodynamic balance rather than by the lip's configuration, as it would be in the case of an open-open pipe.

2. Jet spreading and slowing

In order to determine the position at which the jet is fully developed, l_e, an image analysis algorithm, has been implemented and is described in the Appendix.

Results of l_e are displayed in Fig. 8 (upper graph). The turbulent mechanisms are triggered closer to the flue exit as the Reynolds number increases: from $l_e/h \sim 5$ for $\mathrm{Re} = 2400$ to $l_e/h \sim 2$ for $\mathrm{Re} = 5200$. No apparent relation to angle α or to the jet offset y_{off} is observed.

3. Jets instabilities

The function $\eta_0 e^{\alpha_i x}$ is fitted to the wave amplitude data. The measured amplification factor $\beta = h\alpha_i$ is shown in Fig. 9. The order of magnitude of the growth rate is the same as the ones found in the literature for turbulent jets.[5,18,24] No specific trend with the Reynolds number Re or with angle α has been found. As already observed in these earlier studies, there is no difference between the laminar and turbulent regions. In addition, an interesting result was obtained for the three experiments where $y_{off} \simeq 3$ mm. In this case, the growth rate α_i is larger and shows a dependence on the angle.

Another parameter usually studied together with the amplification factor is the convection velocity c_p, deduced from phase of the wave $\phi_{\eta'}$ with the expression[4]

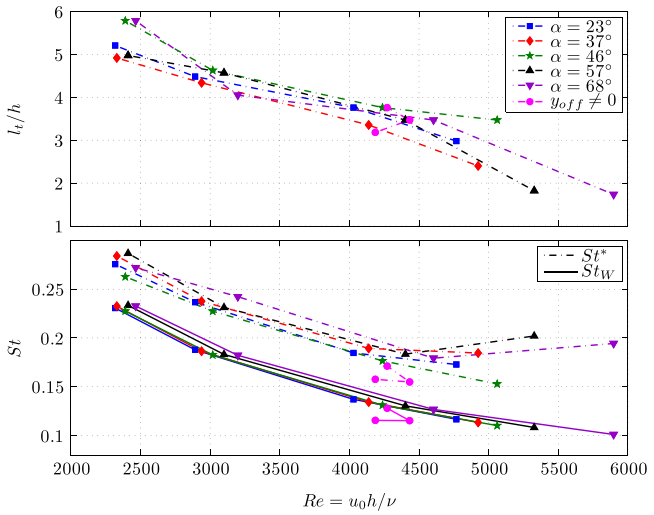

FIG. 8. (Color online) Dimensionless establishment l_e/h and Strouhal numbers $St_W = fW/u_0$ and St^* [see Eq. (12)] versus the Reynolds number $\mathrm{Re} = u_0 h/\nu$ for all the blowing conditions. When not specified in the legend, the offset y_{off} is null.

$c_p = \omega(d\phi_{\eta'}/dx)^{-1}$. It provides information on the total delay, and thus on the ability of the system to overblow. As expected from the model, the rate of change of phase $d\phi_{\eta'}/dx$ behaves differently before and after the establishment length l_e. There is a change in the slope of the phase that coincides with l_e, reducing the phase velocity for the turbulent region. However, the phase data of the present experiment are too noisy (because of turbulence) to allow for a proper estimation of c_p. Only for a few of the experiments it was possible to deduce information on c_p, which was estimated to be in the range of $c_p \propto x^{-0.5}$ to $c_p \propto x^{-2.5}$.

4. Overblowing

Stopped pipes also tolerate a wider range of jet velocities in the first oscillating regime, compared to open pipes. Experimental observations in open pipes show that for a Reynolds number as high as 5200, the Strouhal number $\mathrm{St}_w = fW/u_0$ is expected to reach the overblowing threshold of 0.07. The data collected in the present experiment [Fig. 8 (lower graph)], show that for $\mathrm{Re} \sim 5200$ the lowest value of St_w observed is close to 0.1.

A second Strouhal number St^* [see Eq. (12)] that accounts for the jet slowing is also displayed in Fig. 8. Although it shows the same behavior as St_w, the values of St^* are greater due to a corrected jet velocity, and may be a more accurate measure of the system's ability to overblow. We see that St^* does not decrease below 0.07, value around which the system is expected to overblow. A thorough analysis of this phenomenon demands the careful consideration of the evolution of the central velocity of the jet. As the initial velocity u_0 is raised, turbulent mixing on the jet is triggered closer to the flue and thus the characteristic slowing caused by turbulence has a greater impact. As a consequence, a higher velocity is necessary to achieve the overblowing, which has the musical advantage of allowing a larger dynamic range within the first register. Along with the hydrodynamical consideration, increasing the jet velocity also affects the oscillating frequency, which, in the present experiment, can be increased by as much of one quarter tone.

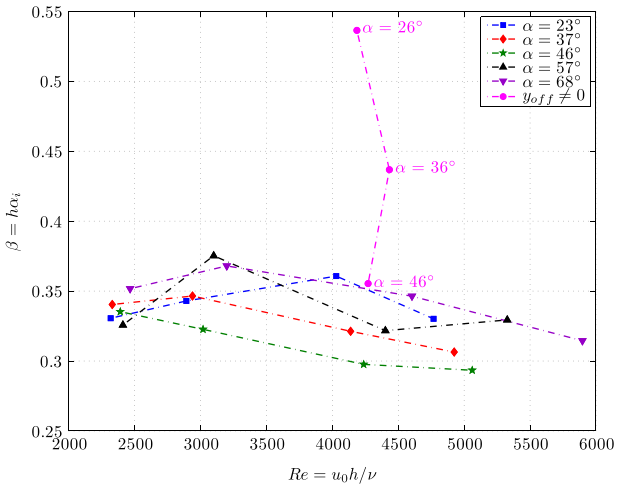

FIG. 9. (Color online) Growth factor $\beta = h\alpha_i$ versus the Reynolds number $\mathrm{Re} = u_0 h/\nu$ for all the blowing conditions. When not specified in the legend, the offset y_{off} is null.

C. Acoustical analysis

Characteristic spectra of the closed end oscillating pressure p' are plotted in Fig. 10 for two different configurations. The spectra show harmonics as well as a strong broadband noise filtered by the resonator. An unexpected antiresonance modulates the broadband noise around 1600 Hz, which is probably a consequence of the visualization window. The broadband noise highlights the response of the resonator and thus the pipe modes become visible in the spectrum. The frequency ratio of the pipe modes follows an approximate relation of odd integers of the fundamental, but toward the higher modes this relation becomes more inharmonic and also depends on the orientation angle of the jet, α.

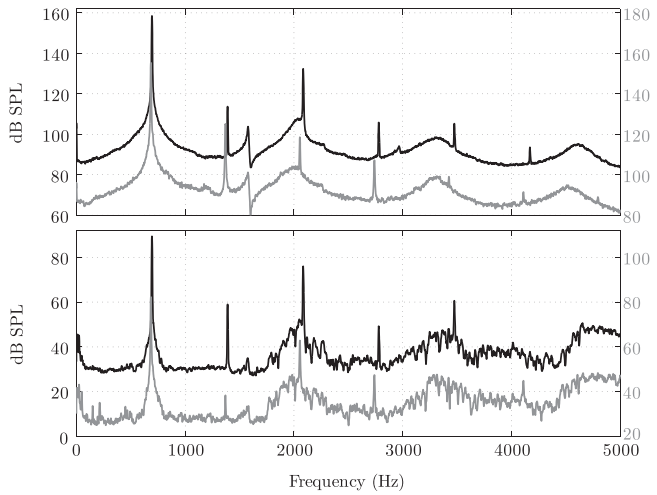

FIG. 10. Spectra of the oscillating part of the pressure at the closed end (top) and of the radiated sound (bottom) for two runs of the experiments: blowing condition $\mathrm{Re} = 5200$, $\alpha = 24°$, $y_{off} = 0$ mm (black) or 3 mm (gray, shifted by -20 dB). The spectra are estimated through a power spectral density using a 8192 point DFT averaged over ~30 windows of length 0.33 s.

Over all the blowing conditions, the fundamental frequency varies around the resonance frequency $f_1 = 686$ Hz (see Fig. 11, top), showing a maximum deviation of $\pm 3\%$ (a quarter tone) for the two extreme conditions [-3% for ($\mathrm{Re} = 2400$, $\alpha = 24°$) and $+3\%$ for ($\mathrm{Re} = 5200$, $\alpha = 69°$)]. The fundamental frequency increases with the Reynolds number and with the aperture of the open end (as the angle α increases).

The spectral content is characterized by the harmonics, odd and even, and the broadband noise. The amplitude of the harmonics is estimated by computing a discrete Fourier transform (DFT) over a window that includes an integer number of oscillation periods (30 periods with a sample rate of 25 kHz). Therefore, the amplitude of each bin of the DFT includes the energy within a band of 22.5 Hz. The broadband noise is estimated by averaging a DFT computed over a much larger window (3000 periods). Harmonics and noise estimation are displayed in Fig. 11 (bottom).

The amplitude of the fundamental is always larger by at least 30 dB than the one of the third (and other) harmonics. The whole spectral content follows the same trend as the fundamental for all the blowing conditions: the amplitude increases with the Reynolds number. The first and third harmonics are higher than the second, which has almost the same level as the noise. When the jet is aimed at the center of the bore (Fig. 10, gray, top), the energy balance between odd and even harmonics is modified: the amplitude of the second harmonic exceeds that of the third. However, even harmonics are radiated less effectively than odd ones: for the case $y_{off} = 3$ mm (Fig. 10, gray, bottom), the second harmonic of the radiated sound is lower than the third one whereas this is reversed for the internal pressure signal. This could be explained by the fact that, for an odd harmonic, the pressure node at the open end (pipe termination) corresponds to a velocity antinode. For even harmonics one would actually expect a velocity antinode at the open end. The radiation is determined by the acoustic volume flux at the open end rather than the pressure at the closed end of the pipe, where pressure is actually measured.

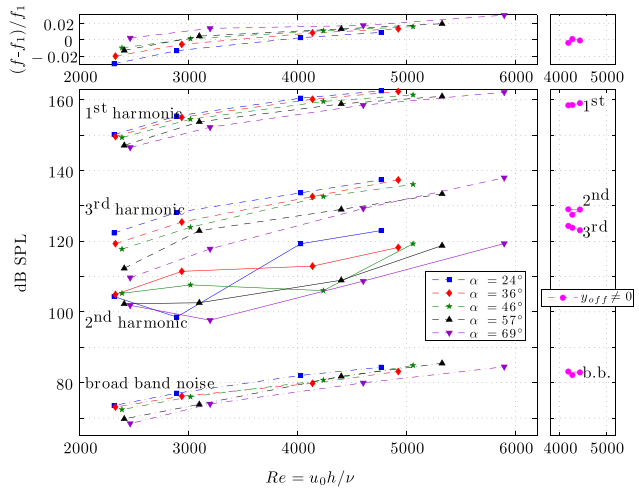

FIG. 11. (Color online) Deviation in the fundamental frequency $(f - f_1)/f_1$ with $f_1 = 686$ Hz (top) and harmonics and broadband noise levels of the internal pressure p' (bottom) versus the Reynolds number $\mathrm{Re} = u_0 h/W$ (dashed lines: first and third harmonics; solid lines: second harmonics; dashed-dotted lines: broadband noise). When not specified in the legend, the offset y_{off} is null. For the case $y_{off} \neq 0$, the second harmonics are higher than the third ones.

The amplitude of oscillation of the pressure at the closed end p' makes it possible to estimate the ratio of the acoustic velocity over the jet velocity through the dimensionless amplitude proposed by Verge *et al.*[25] $p'_1/\rho c_0 u_0$, where p'_1 is the amplitude of the fundamental. The dimensionless amplitude is displayed in Fig. 12. It slightly increases with the Reynolds number but remains under the usual value, ~ 0.2, found by other authors for different types of flutes and blowing conditions. Note that $p'_1/\rho c_0 u_0$ does depend on the ratio of jet length to jet thickness (see Verge *et al.*[25]). Additionally, a clear consequence of the variation of the angle α is observed: for a jet directed towards the labium, the amplitude of oscillation increases about 5 dB as the angle decreases from 69° to 24° (the jet aligns with the pipe axis).

V. CONCLUSIONS

Some fundamental aspects of the hydrodynamics of stopped end pipes have been discussed analytically and observed in a controlled experiment. The musician has direct control over several parameters, such as the jet-labium offset y_{off}, the central velocity of the jet u_0, and the jet-pipe angle α. Changes in any of these three parameters have an incidence on the hydrodynamic behavior and thereby on the acoustic behavior. We have observed that a wide range of these parameters produces sound.

The turbulent jet instability was measured observing that the growth rate for a transversal perturbation is of the same order of magnitude as for a laminar jet ($\beta = h\alpha_i \simeq 0.24$). The amplification coefficient α_i is larger when the jet is directed to the center of the bore ($\beta = h\alpha_i \sim 0.25$ to 0.38), also displaying a dependence on the jet-pipe angle α. The jet's central velocity is constant in the laminar jet core but decreases according to $u_0 \propto x^{-1/2}$ and also spreads linearly with x in the fully developed turbulent region.[18] The velocity of convection of the perturbation (c_p), which depends on the jet's central velocity, is affected by the regime

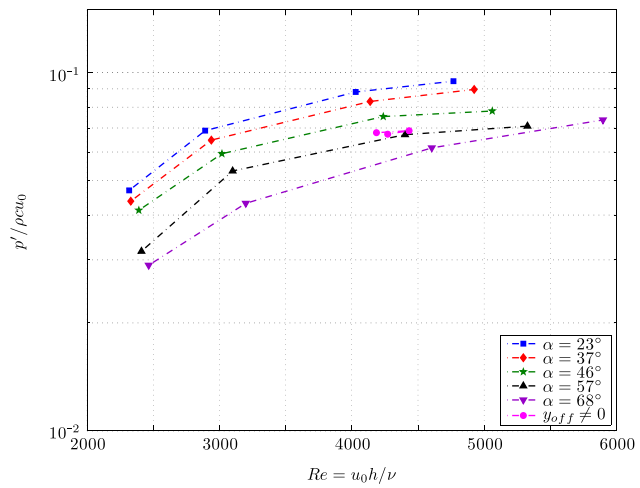

FIG. 12. (Color online) Dimensionless amplitude of oscillation $p'/\rho_0 c_0 u_0$ versus the Reynolds number $\mathrm{Re} = u_0 h/W$. When not specified in the legend, the offset y_{off} is null.

transition and shows an x-dependence similar to the one expected for the centerline velocity u_0.

A remarkable observation has to do with the auto-direction of the jet toward the labium in stopped pipes. The player does not need to aim the jet directly at the labium in order to produce a stable oscillation. This behavior has already been predicted theoretically[2] and is now measured experimentally.

The effect of the crossflow was successfully modeled as a deviation of the jet's centerline with a polynomial dependence on the horizontal distance $\langle\eta\rangle/rh = a(x/rh)^{\delta}$, with $\delta \simeq 2$. The model proved to be valid for the first half of the jet length. The magnitude of this deviation depends strongly on the jet-labium offset.

Any change in the symmetrical properties of the nonlinear exciter is known to affect the relative strength of the harmonics. This is the case of the offset between the jet axis and the labium.[30] Although in stopped pipes part of this offset is corrected by the steady deflection, the equilibrium point of the oscillating jet is still slightly off the labium, producing an asymmetrical jet impact. The deflection mechanism makes it possible to produce stable oscillations for a large range of jet offsets, while maintaining the ability to control the harmonic generation as it can be performed on a lip-blown open-open pipe, such as the transverse flute.

Additionally, a wide range of angles at which the pipe is able to produce stable oscillations is observed. Both the oscillating frequency and the acoustic power are correlated with this angle.

Thus, from the standpoint of the musician, the production of a tone in a stopped pipe seems easier than in the case of an open-open flue instrument. This might partly explain why stopped pipes were the most common type of resonator found in ancient civilizations in the region.

ACKNOWLEDGMENTS

The authors would like to thank Tristan Cambonie for sharing his knowledge about the intricate issue of jets in crossflow, Arnaud Gérard for providing musical excerpts of siku, and the reviewers for their relevant and useful corrections and suggestions. The work undertaken for this study has been possible thanks to the support of FONDECYT (Grant No. 1161464), CONICYT, Government of Chile.

APPENDIX: IMAGES PROCESSING

Pre-processing the data. The camera frame rate is much lower than the frequency of the jet wave (8 Hz and ~690 Hz, respectively) so that sequential images do not follow the oscillating motion of the jet. However, large-scale patterns of vorticity are phase-locked with the acoustic oscillations, as mentioned in Sec. II B 3. An algorithm was developed to label images with the instantaneous phase of the fluctuating pressure at the closed end p' at the moment of their capture. Thus, an array of images $I = [I_1, I_2, ..., I_N]$ is linked to a vector of phases $\phi = [\phi_1, \phi_2, ..., \phi_N]$ which are distributed uniformly in the interval $[0 - 2\pi]$. The array I and the vector ϕ are reordered so that $0 \leq \phi_1 \leq \phi_2 \leq \cdots \leq \phi_N < 2\pi$.

Small scale patterns of vorticity have no relation to the acoustic oscillations and behave randomly in consecutive images of I. This complicates the analysis from the viewpoint of the detection of the centerline. By aggregating information from phase adjacent images, recurrent structures are highlighted and others decomposed. The following pixel-by-pixel procedure combines images in I using a Gaussian-weighted average around a phase φ. The result is called an aggregated image $\tilde{J}(\varphi)$:

$$\tilde{J}(\varphi) = \frac{\sum_{k=1}^{N} I_k \cdot c_k(\varphi)}{\sum_{k=1}^{N} c_k(\varphi)}, \tag{A1}$$

where the coefficients $c_k(\varphi)$ are defined as

$$c_k(\varphi) = e^{-1/2((\phi_k - \varphi)/\zeta)^2}, \tag{A2}$$

and the parameter ζ adjusts the spread of the curve.

A reconstruction in time of a period of oscillation of the jet wave is made in M uniform frames $0, (1/M)2\pi, ..., ((M-1)/M)2\pi$. Aggregated images $\tilde{J}(\varphi)$ are computed by forcing φ to match those intervals, and single-shot images J are picked out as uniformly as possible from ϕ.

For the following analysis, parameters are set to $\zeta = 8.4°$ and $M = 32$.

Prior to the subsequent analysis of the jet's centerline, the main axes of the model (see Figs. 3 and 13) have to be defined. To this effect, an x axis and a representative point marking the origin of the jet must be found. The former cannot be deduced from images for these contain information on the vertical displacement. However, the total average of images in array $\tilde{J}$ is expected to provide a better idea of the initial orientation of the jet. A line is adjusted to fit the direction of the early development of the jet, and the origin is placed at the edge of the flue. In order to generalize the axes

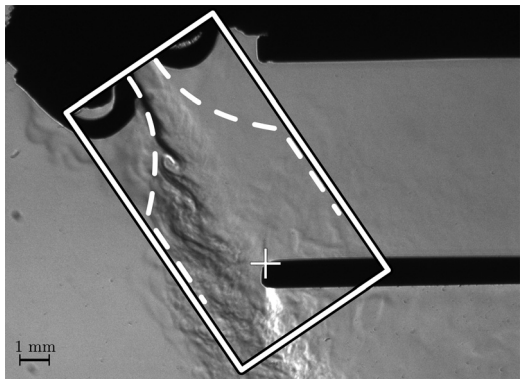

FIG. 13. Typical image captured by the camera for the blowing condition (Re,α) = (3000,57°). The rectangle is the window of observation, the dashed line is the mask used for the detection of the jet transverse oscillation, and the white cross is the center of rotation on which the jet axis is centered.

definition for different geometrical configurations, it is necessary to develop an alignment algorithm that uses the structure of the nozzle as an invariant marker of the orientation of the jet. The algorithm is based on the technique called "image registration," which maximizes the mutual information between images,[29] and yields the translation and rotation of the nozzle structure relative to a reference. Thus, the axes need to be defined for one experiment only, and the results are extrapolated to the rest by means of the alignment algorithm.

Jet centerline tracking: Relative displacement. De la Cuadra[5] proposed an algorithm for measuring the vertical displacement of a jet based on the cross-correlation between analog gray profiles of images at consecutive time frames. The method uses a reference image and cross-correlates the rest to it. Thus, displacements obtained are relative to the one in the reference image. A brief summary of the algorithm is provided below.

The cross-correlation of a vertical gray profile $l(y,x,t)$ at a distance x from the flue and time frame t is

$$X(y,x,t) = \int_{-\infty}^{\infty} l(y-\tilde{y},x,t_{ref})l(\tilde{y},x,t)d\tilde{y}. \tag{A3}$$

$X(y,x,t)$ will have a maximum for a lag $\tilde{y}$ that makes both profiles match best. Then, the shift of that maximum from the center of the vector is taken as the relative displacement $\tilde{\eta}(x,t)$. This is often on the order of a few pixels, so that the parabolic interpolation of the three highest values is used to increase resolution of the peak detection.

This operation is repeated for the M time frames and for the entire discrete window of N_W points ($x \in [0, N_W - 1]$). The result of the algorithm is the $M \times N_W$ matrix of relative displacements whose first row is made up of zeros to represent the unknown displacement of the reference image.

Jet centerline tracking: Absolute displacement. In open-open pipes, the mean deflection of the centerline $\langle\eta\rangle$ coincides with the x axis. This makes it possible to correct the reference displacement by forcing the mean value of the columns of $\tilde{\eta}(x,t)$ to zero. In stopped pipes $\langle\eta\rangle$ varies with x; hence, the position of the jet in the reference image must be obtained separately and it must then be subtracted from $\tilde{\eta}(x,t)$.

The morphology of the jet in aggregated images is characterized by two velocity profiles (a top-hat shaped profile at the exit of the nozzle, and an auto similar profile a distance away from it). First, the shear layers are two distinguishable boundaries of the jet, and after a certain distance of establishment l_e, these boundaries collapse in the centerline. Two algorithms based on vertical gray profiles run in the regions $x \in [0, \tilde{l_e} - 1]$ and $x \in [\tilde{l_e}, N_W - 1]$, respectively, where the distance $\tilde{l_e}$ is a heuristic estimation of l_e used only for this transition. Despite the gradual nature of the diffusion of the shear layers, the change is assumed—without compromising the results—to be discrete.

In the first region, a profile $l(y,x,t)$ looks like Fig. 14 (upper graph). Maximum and minimum points are good indicators of the boundaries of the jet, and the centerline is assumed to lie at the center of both.

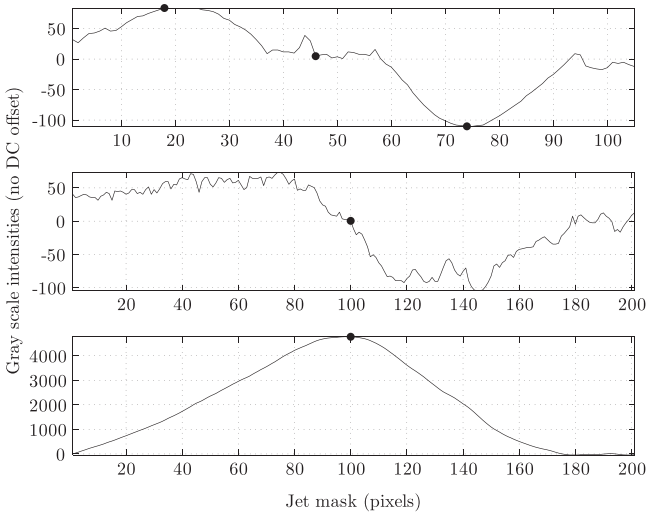

FIG. 14. (a) Gray profile in laminar region. (b) Gray profile in turbulent region. (c) Integral of (b).

A gray profile in the second region looks like Fig. 14 (middle graph). Visualization is now characterized by noise, so that the former criteria of detection are no longer valid. The shape of $l(y,x,t)$ suggests that a larger scale approach is necessary, such as the area below the curve. This operation acts as a low pass filter, reducing the effects of noise. The integral of the gray profile, starting from the first intensity value, is shown in Fig. 14 (lower graph). The maximum of this curve marks the centerline.

An exponential fit to the combined results yields the absolute displacement of the reference image $\eta(x,0)$. Finally, the rows of matrix $\tilde{\eta}(x,t)$ have to be corrected by means of the operation,

$$\eta(x,t) = \eta(x,0) - \tilde{\eta}(x,t), \quad \forall t \in [\![1, M-1]\!]. \tag{A4}$$

A three-dimensional plot of the absolute displacement $\eta(x,t)$ is shown in Fig. 15.

Detection in aggregated images is robust; the centerline can be tracked from the flue to the labium. Therefore, the analysis of the instability of the jet and the mean deflection

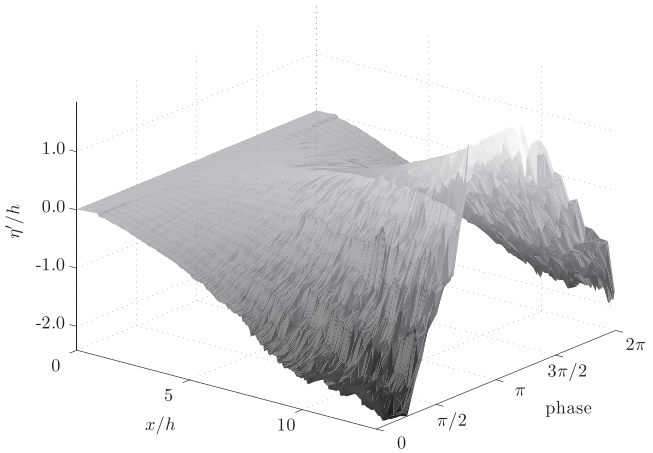

FIG. 15. Three-dimensional representation of the jet transverse oscillation $\eta(x,t)$ versus the M = 32 time frames and the distance from the nozzle x for the case (Re,α) = (4300,36°).

will use these images. Contrarily, algorithms of detection in single-shot images perform poorly due to uncorrelated small-scale patterns of vorticity. This characteristic will be used to identify the establishment length at which the turbulence reaches the core of the jet.

Spatiotemporal analysis of the centerline. The static and oscillatory components of the columns of $\eta(x,t)$ represent the mean jet deflection $\langle\eta\rangle$ and the jet wave $\eta'(x,t)$, respectively. Fourier analysis of the columns of $\eta'(x,t)$ yields the amplitude $|\eta'|$ and the phase $\phi_{\eta'}$. The growth rate α_i is obtained from the fit of $|\eta'|$ using the function $\eta_0 e^{\alpha_i}$, as illustrated in Fig. 16. The convection velocity is deduced from the phase of the wave $\phi_{\eta'}$, with the expression[4] $c_p = \omega(d_x\phi_{\eta'})^{-1}$. c_p depends on the derivate of a noisy vector; thus, it cannot be obtained directly and requires a function to be fit the to $\phi_{\eta'}$ previously. In turbulent jets $c_p \propto x^{-1/2}$, thus $\phi_{\eta'} \propto x^{1/2}$. However, the data obtained are too irregular to generalize a result and requires further investigation. Nevertheless, a change of slope in $\phi_{\eta'}$ that coincides with the detection of the establishment length l_e is observed. In the laminar region, the slope seems to be linear, while in the turbulent region it is better approximated by a polynomial.

Small-scale patterns of vorticity reduce the performance of detection, especially in single-shot images. A measure of turbulence is the mean squared error (MSE) between the normalized columns of $\eta'(x,t)$ and their sinusoidal fit,

$$\mathrm{MSE} = \frac{1}{M}\sum_{t=1}^{M}\left[\frac{1}{|\eta'|(x)}\eta'(x,t) - \cos\left(2\pi M^{-1}t + \phi'_{\eta'}(x)\right)\right]^2. \tag{A5}$$

The MSE can be divided into three regions: forming, laminar and turbulent. Oscillations starts to arise in a region of length $x \sim h$ near the flue exit; this causes the detection to be highly irregular, having a large MSE. In the laminar core region, the MSE quickly decreases due to a structured and cohesive jet. This state lasts until turbulence arises at $x/h \sim 3$–5, depending on the blowing conditions, where the MSE increases rapidly. This establishment length l_e can be easily identified, as shown in Fig. 16 (lower graph), and it was detected heuristically.

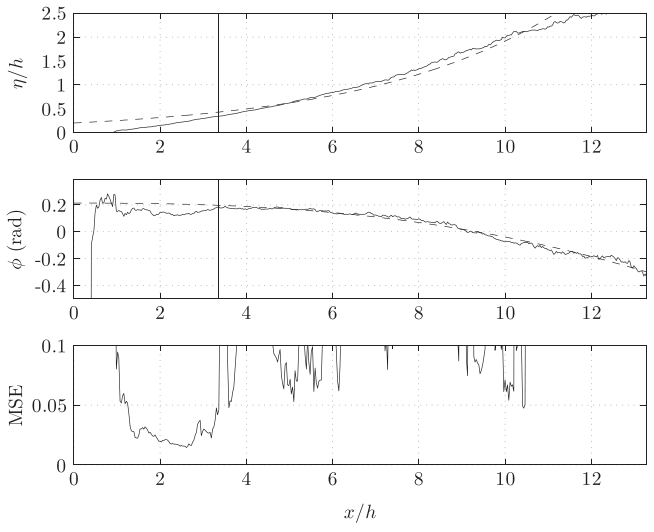

FIG. 16. Amplitude, phase, and MSE of the oscillation of the jet for one blowing condition: (Re,α) = (4300,36°). The vertical line is the estimation of the establishment length l_e based on the MSE.

[1]J. P. de Arce, "Sonido Rajado: The sacred sound of Chilean pifilca flutes," Galpin Soc. J. **51**, 17–50 (1998).
[2]N. H. Fletcher, "Stopped-pipe wind instruments: Acoustics of the panpipes," J. Acoust. Soc. Am. **117**, 370–374 (2005).
[3]B. Fabre, J. Gilbert, A. Hirschberg, and X. Pelorson, "Aeroacoustics of musical instruments," Ann. Rev. Fluid Mech. **44**, 1–25 (2012).
[4]A. W. Nolle, "Sinuous instability of a planar air jet: Propagation parameters and acoustic excitation," J. Acoust. Soc. Am. **103**, 3690–3705 (1998).
[5]P. de la Cuadra, C. Vergez, and B. Fabre, "Visualization and analysis of jet oscillation under transverse acoustic perturbation," J. Flow Visu. Image Proc. **14**, 355–374 (2007).
[6]J. W. Coltman, "Sounding mechanism of the flute and organ pipe," J. Acoust. Soc. Am. **44**, 983–992 (1968).
[7]S. A. Elder, "On the mechanism of sound production in organ pipes," J. Acoust. Soc. Am. **54**, 1554–1564 (1973).
[8]N. H. Fletcher, "Sound production by organ flue pipes," J. Acoust. Soc. Am. **60**, 926–936 (1976).
[9]M.-P. Verge, B. Fabre, W. E. A. Mahu, A. Hirschberg, R. R. van Hassel, A. P. J. Wijnands, J. J. de Vries, and C. J. Hogendoorn, "Jet formation and jet velocity fluctuations in a flue organ pipe," J. Acoust. Soc. Am. **95**, 1119–1132 (1994).
[10]B. Fabre and A. Hirschberg, "Physical modeling of flue instruments: A review of lumped models," Acust. Acta Acust. **86**, 599–610 (2000).
[11]S. Muppidi and K. Mahesh, "Study of trajectories of jets in crossflow using direct numerical simulations," J. Fluid Mech. **530**, 81–100 (2005).
[12]M. W. Plesniak and D. M. Cusano, "Scalar mixing in a confined rectangular jet in crossflow," J. Fluid Mech. **524**, 1–45 (2005).
[13]T. Cambonie, N. Gautier, and J.-L. Aider, "Experimental study of counter-rotating vortex pair trajectories induced by a round jet in cross-flow at low velocity ratios," Exp. Fluids **54**, 1–13 (2013).
[14]S. H. Smith and M. G. Mungal, "Mixing, structure and scaling of the jet in crossflow," J. Fluid Mech. **357**, 83–122 (1998).
[15]T. H. New, T. T. Lim, and S. C. Luo, "Effects of jet velocity profiles on a round jet in cross-flow," Exp. Fluids **40**, 859–875 (2006).
[16]T. H. New, T. T. Lim, and S. C. Luo, "Elliptic jets in cross-flow," J. Fluid Mech. **494**, 119–140 (2003).
[17]D. J. Tritton, *Physical Fluid Dynamics*, 2nd ed. (Oxford University Press, Oxford, 1988), Chaps. XVIII, XXI.
[18]S. Thwaites and N. H. Fletcher, "Wave propagation on turbulent jets," Acustica **45**, 175–179 (1980).
[19]G. E. Mattingly and W. O. Criminale, "Disturbance characteristics in a plane jet," Phys. Fluid **14**, 2258–2264 (1971).
[20]D. G. Crighton and M. Gaster, "Stability of slowly diverging jet flow," J. Fluid Mech. **77**, 397–413 (1976).
[21]P. de la Cuadra, "The sound of oscillating air jets: Physics, modeling and simulation in flute-like instruments," Ph.D. thesis, University of Stanford, 2005.
[22]R. Auvray, P.-Y. Lagrée, and B. Fabre, "Regime change and oscillation thresholds in recorder-like instruments," J. Acoust. Soc. Am. **131**, 1574–1585 (2012).
[23]J.-C. Lin and D. Rockwell, "Oscillations of turbulent jet incident upon an edge," J. Fluid Struct. **15**, 791–829 (2001).
[24]S. Thwaites and N. H. Fletcher, "Wave propagation on turbulent jets: II. Growth," Acustica **51**, 44–49 (1982).
[25]M.-P. Verge, B. Fabre, and A. P. J. Wijnands, "Sound production in recorderlike instruments. I. Dimensionless amplitude of the internal acoustic field," J. Acoust. Soc. Am. **101**, 2914–2924 (1997).
[26]C. Ségoufin, B. Fabre, M.-P. Verge, A. Hirschberg, and R. Caussé, "Experimental study of the influence of the mouth geometry on sound production," Acust. Acta Acust. **86**, 649–661 (2000).
[27]P. de la Cuadra, B. Fabre, N. Montgermont, and C. Chafe, "Analysis of flute control parameters: A comparison between a novice and an experienced flautist," Acust. Acta Acust. **94**, 740–749 (2008).
[28]H. Schlichting and K. Gersten, *Boundary Layer Theory*, 8th ed. (Springer-Verlag, Berlin, 2004), Chap. XX.
[29]F. Maes, A. Collingnon, D. Vandermeulen, G. Marcha, and P. Suetens, "Multimodality image registration by maximization of mutual information," IEEE Trans. Med. Imag. **16**, 187–198 (1997).
[30]N. H. Fletcher and L. M. Douglas, "Harmonic generation in organ pipes, recorders, and flutes," J. Acoust. Soc. Am. **68**, 767–771 (1980).